43 p.

NASA TN D-1391

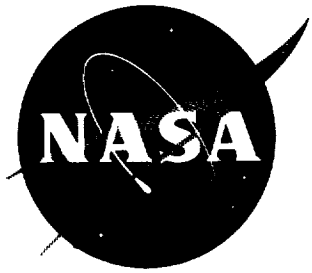

TECHNICAL NOTE

D-1391

WIND-TUNNEL MEASUREMENTS OF AERODYNAMIC DAMPING DERIVATIVES OF A LAUNCH VEHICLE VIBRATING IN FREE-FREE BENDING MODES AT MACH NUMBERS FROM 0.70 TO 2.87 AND COMPARISONS WITH THEORY

By Perry W. Hanson and Robert V. Doggett, Jr.

Langley Research Center
Langley Station, Hampton, Va.

NATIONAL AERONAUTICS AND SPACE ADMINISTRATION

WASHINGTON October 1962

NATIONAL AERONAUTICS AND SPACE ADMINISTRATION

TECHNICAL NOTE D-1391

WIND-TUNNEL MEASUREMENTS OF AERODYNAMIC DAMPING DERIVATIVES OF A LAUNCH VEHICLE VIBRATING IN FREE-FREE BENDING MODES AT MACH NUMBERS FROM 0.70 TO 2.87 AND COMPARISONS WITH THEORY

By Perry W. Hanson and Robert V. Doggett, Jr.

SUMMARY

The aerodynamic damping of a flexibly mounted aeroelastic model with a blunted conical nose and a cylindrical afterbody was measured at Mach numbers from 0.70 to 1.20 at several levels of dynamic pressure and two weight conditions and at Mach numbers from 1.76 to 2.87 at one weight condition. The first two free-free flexible modes of vibration were investigated. Also investigated at Mach numbers from 0.9 to 1.2 was the aerodynamic damping in the first free-free modes of a model which had a "hammerhead" nose (the base diameter of the blunted cone was greater than the diameter of the afterbody which necessitated a reflex angle downstream from the cone base).

Two basically different methods, the "electrical power-input" and the "decaying oscillations" methods were used to determine the damping and frequencies. The experimentally determined values are compared with some applicable theories. The results of the investigation indicate that the aerodynamic damping in the elastic modes of vibration was small for all configurations tested. The maximum aerodynamic damping measured in the first mode was on the order of 60 percent of the structural damping. The aerodynamic damping was found to be even less for vibration modes higher than the first. Reduced-frequency effects were found to be negligible for the range investigated. Agreement of calculated aerodynamic damping derivatives with the experimental results was not good. Generally, the experimentally determined derivatives were larger than those predicted by the various theories used. The Bond-Packard theory appeared to give the best agreement for the first free-free vibration mode but gave the worst agreement for the second mode. Measurements made on the configuration that had a hammerhead nose indicated small negative aerodynamic damping in the Mach number range from 0.95 to 1.00. Aerodynamic stiffness effects were found to be small and within the experimental scatter. (Wind-on frequency determination was accurate only to approximately 1 percent.)

INTRODUCTION

The problem of the determination of oscillatory aerodynamic derivatives of aircraft and/or aircraft components has been met to some extent by the use of theoretical estimates and a number of derivative measurements. However, comparatively little work has been done on this problem as related to slender bodies of revolution representative of guided missiles and space launch vehicles, particularly in the experimental field. Launch vehicles, especially, are structures of maximum design efficiency with a minimum of weight available for supporting members. The resulting structures are relatively flexible and could be subject to aeroelastic instabilities particularly in the cases where lifting payloads are involved. The need for suitable theoretical approaches and experimental data on the oscillatory aerodynamic derivatives of such slender bodies of revolution is thus becoming more urgent. The lack of experimental data, both as an indication of the magnitudes of the derivatives involved for flexible slender bodies of revolution and as a basis for evaluating the accuracy of theoretical predictions, is therefore of increasing concern.

It is for this reason that the present investigation was undertaken to attempt to measure experimentally the aerodynamic damping and stiffness of an aeroelastic model having scaled physical properties approximating those of a launch vehicle. The purpose of the investigation was twofold: first, to attempt to apply some known general techniques of measurement of oscillatory aerodynamic derivatives to the rather specialized problem at hand; and second, to present the results of the investigation as an indication of the relative accuracy of several theoretical approaches that might be used.

There are, of course, many methods that may be employed for the measurement of aerodynamic derivatives in wind tunnels. Reference 1 presents a rather complete discussion of various methods that have been used in the past and contains an extensive list of references on the subject. For the present investigation, it was decided that, because of the expected small values of the derivatives with the attendant difficulty of accurate measurement, two basic techniques would be used concurrently. One technique chosen was the "power-input" method where the model is excited at resonance with an electromagnetic shaker. The other technique chosen was the well-known "decaying oscillation" method. In both techniques the aerodynamic stiffness is indicated by the change in frequency between the wind-on and the wind-off conditions.

Tests were conducted in the Langley 8-foot transonic pressure tunnel over the Mach number range from 0.70 to 1.20 and in the Langley Unitary Plan wind tunnel over the Mach number range from 1.76 to 2.87. The basic model was a slender cone cylinder designed to approximate the geometric and dynamic characteristics of a representative launch vehicle.

Tests were also conducted on a model having natural frequencies approximately twice those of the basic scaled model and on a model where the conical nose was replaced with a "hammerhead" type nose.

Several aerodynamic theories (refs. 2 to 7) were used to calculate predicted aerodynamic damping coefficients. The results are compared with the experimental results.

SYMBOLS

A_C distribution function of damping portion of aerodynamic loading

A_I distribution function of inertia portion of aerodynamic loading

A_K distribution function of stiffness portion of aerodynamic loading

$a(t), b(t)$ tip amplitudes

B, C generalized damping

c damping per unit length

C_{cr} critical value of damping

$C_{\dot{h}}$ damping derivative $\left(C_{\dot{h}} = 2\mu k \frac{C_A}{C_{cr}}\right)$

$C_{N,\alpha}$ section steady-state normal-force slope

EI flexural stiffness

$F(t)$ sinusoidal driving force

F generalized aerodynamic force

G_1, G_2 functions of M_∞ and θ

h_0 amplitude of decaying vibration

h_p amplitude of decaying vibration after p cycles

$h(x), H(x)$ mode shapes based on unit tip deflection

I current

K	generalized stiffness
k_1, k_2	spring constants
L	length of model
M	generalized mass
M_∞	free-stream Mach number
$m(x)$	mass per unit length
m, n	integers
P	electrical power
p	number of cycles between amplitudes h_0 and h_p
q	dynamic pressure, $\frac{1}{2}\rho V^2$
q_1, q_2	proportionality constants
$Q_h^{\cdot}$	generalized force associated with aerodynamic damping
R	electrical resistance
$R(x)$	function defining model geometry
r	radius of cylindrical portion of model
t	time
T	arbitrary period of time
V	free-stream velocity
$W(x,t)$	aerodynamic running shear load
x, y	Cartesian coordinates
$y(x,t)$	deflection shapes
x_1, x_2	longitudinal locations of springs k_1 and k_2, respectively
x_3	longitudinal location of applied sinusoidal force, $F(t)$
α	angle of attack

δb virtual displacement

δW_A virtual work done by aerodynamic forces

$\delta(x-x_n)$ Dirac function

γ ratio of specific heats

θ cone semivertex angle

ρ test medium density

μ mass ratio $\left(\mu = \frac{M_s}{\rho\pi r^2 L}\right)$

λ,Ω,ω circular frequencies

Subscripts:

m mth natural vibration mode, m = 1, 2, 3, . . .

n nth natural vibration mode, n = 1, 2, 3, . . .

A aerodynamic

r random quantities

s structural

Dots over symbols indicate derivatives with respect to time.

APPARATUS AND TEST PROCEDURE

Model and Support System

Construction.- The construction of the model and sting used in the tests is illustrated in figures 1, 2, and 3. The model was built in three sections to make insertion of instrumentation and ballast weights easier and to permit easier assembly on the sting. Basically, each section consisted of a fiber-glass shell 0.03 inch thick bonded to aluminum rings which served to stiffen the model in the hoop plane. The rings also were used as mounts for the accelerometers, shaker moving coils, the flex springs which supported the model on the sting, and the lead weights which were used to lower the natural vibration frequencies to scaled values approximating those that might be considered typical of launch vehicles. Model dimensions are presented in figure 2.

The model was supported on the sting by the flex springs shown in figure 3. These springs were located approximately at the first free-free node points on the model in order to minimize their influence on the free-free modes.

The model was excited in its natural free-free modes of vibration by the electromagnetic shaker built into the sting. Also incorporated in the sting was a provision for cooling the shaker by means of circulating cooling air through the sting and blowing it back on the field coils. The sting also carried a set of pneumatic brakes which were used to restrain the model during starting and stopping transient flow. These features are shown in figure 1(b). The basic model mounted in the Langley Unitary Plan wind tunnel is shown in figure 4.

Model physical properties.- Three model configurations were tested. Configurations 1 and 2 differed only in the mass, the model geometry being the same. Configuration 3, however, consisted of the basic model with a large hammerhead nose which was fitted over the basic shell in such a manner that it touched the basic shell only at the nose and shoulder. (See fig. 2.) The experimentally determined frequencies, mode shapes, and damping ratios of the three configurations are presented in table I and figure 5. Also presented in figure 5 are the calculated mode shapes for a uniform free-free beam. As is shown by the figure the mode shapes for the models tested in this investigation are very similar to those of a uniform free-free beam. These mode shapes were determined through the use of a small velocity pick-up. The mass distribution, determined by weighing the individual components before assembly, is shown in table II. Also shown are the total weights of the configurations, the calculated generalized masses, the natural frequencies of vibration, and the values of critical damping.

INSTRUMENTATION

The model instrumentation consisted of an accelerometer located in the nose which was used to indicate the shaking amplitude of the model; two skin thermocouples located approximately at one-quarter and three-quarters of the model length; and electrical wire resistance type strain gages located on the flex springs. Thermocouples also were imbedded in the moving coils and field coils of the shaker in order to provide a means for monitoring the coil temperatures. An accelerometer on the end of the sting provided a means of determining vertical sting motion.

A variable-frequency oscillator and power amplifier were used to provide alternating current to the moving coils and a direct-current variable voltage transformer supplied the direct current to the shaker field coils. A fouling light provided a means of determining that the moving coils were riding free of the stationary parts of the shaker.

The readout instrumentation consisted of the following:

Vacuum tube voltmeter: indicated model vibration amplitude from accelerometer in mode nose

Ammeter: indicated current applied to moving coils of shaker

Ammeter: indicated current applied to field coils of shaker (held constant at 2.5 amps)

Low-power-factor wattmeter: indicated power drawn by moving coils

Oscilloscope: provided means for monitoring wave form of force output of shaker and of model response

Electronic period counter: used to determine frequency of forced oscillations

Potentiometer: indicated temperature of the model skin, the moving coils, and the field coils

Electronic dampometer: measured the logarithmic decrement and the decaying frequency and was used to monitor the damping in order to determine any large changes due to structural failure. This electronic device is described in reference 8.

Oscillograph: recorded the signals from the accelerometer in the model nose, the strain gages on the model supporting flex springs, and the fouling indicator.

A block diagram of the instrumentation setup is shown in figure 6. A variable-frequency voltage was applied to the shaker moving coils by an oscillator and a power amplifier. A constant current of 2.5 amperes was supplied to the shaker field coils by a d-c power supply. The current through the moving coils was measured by use of a vacuum-tube voltmeter shunted with a 1-ohm precision resistor. The power consumed by the shaker was measured by use of a low-power-factor wattmeter. A supplementary circuit was employed to determine accurately the resistance of the moving coils which varied due to temperature changes in the coils. Immediately after each test point, a battery-supplied voltage was applied to the coils and the voltage and corresponding current noted from the voltmeter and ammeter, respectively.

Wind Tunnels

The investigation was conducted in two wind tunnels. The Langley 8-foot transonic pressure tunnel was used for the Mach number range from 0.8 to 1.2 and the Langley Unitary Plan wind tunnel was used for the Mach number range from 1.76 to 2.87. Both tunnels are of the continuous-flow type with variable Mach number and density control. Stagnation temperature in both tunnels was held constant at approximately 125° F.

Test Procedure

The test procedure used in both tunnels was essentially the same. After mounting the model in the tunnel it was shaken at the resonant frequency of the desired free-free mode with no air flowing at several test-section pressures from atmospheric down to moderately low vacuums with cooling air on and off. No change in frequency or damping was observed. While the model was vibrating at a given amplitude, data were recorded from all the meters necessary for application of the "power-input" method of determining damping. The power to the shaker was then cut (and the shaker moving coils removed from the electrical circuit) and the decaying oscillations of the model were recorded. While the model motion was decaying, the logarithmic decrement and decaying frequency were measured by an electronic dampometer. This device provided a quick means of detecting any extreme changes in damping due to structural failure, loose screws, and so forth. After obtaining the no-wind data, the model "brake" was actuated and the tunnel started. When the tunnel reached the desired operating conditions, the model brake was released and the above procedure repeated. The process was continued for all the modes investigated at the various Mach numbers and at several levels of dynamic pressure at each Mach number. The Reynolds number range for the tests was from 0.7×10^6 to 2×10^6 based on model afterbody diameter.

Reduction of Data

The method of calculating damping from freely decaying motions of a structure is well known. The ratio of total damping to critical damping for a given mode of vibration of a linear system is

$$\frac{C_A + C_s}{C_{cr}} = \frac{1}{2\pi p} \log_e \frac{h_0}{h_p}$$

where

h_0 an amplitude of vibration

h_p amplitude of vibration after p cycles

p number of cycles between amplitude h_0 and h_p

The aerodynamic damping ratio $\frac{C_A}{C_{cr}}$ is determined by measuring the structural damping ratio $\frac{C_s}{C_{cr}}$ in still air before each test and subtracting it from the total damping measured during the test.

Relationships for determining the damping ratio from the elctrical measurements are developed in appendix A. The resulting expression is

$$\frac{C_A + C_s}{C_{cr}} = \frac{q_1^2 H(x_3)}{2q_2 M_s \lambda} \frac{I^2}{P - I^2 R}$$

(see appendix A) where

$H(x_3)$ mode-shape deflection at shaker location

I current through shaker moving coils

M_s generalized mass of model

P electric power consumed by shaker moving coil circuit

q_1 proportionality constant relating shaker force output to the current applied to moving coils

q_2 a proportionality constant relating model tip velocity to voltage applied to moving coils

R electrical resistance of shaker moving coil circuitry

λ natural vibration frequency at test condition

Since the ratio of structural damping to critical damping of the model was found to be slightly dependent upon amplitude and temperature, it was necessary to construct calibration curves of structural damping ratios against model-vibration amplitude and skin temperature so that structural damping measured before the tests could be corrected to correspond to that associated with the vibration amplitude and skin temperature of the model at the test point. A representative set of these calibration curves is shown in figure 7. After adjusting the no-wind structural damping to the value associated with the wind-on test point, the adjusted structural damping ratio was subtracted from the wind-on total damping measured to get the aerodynamic damping ratio. For convenience in presenting the data, an averaged value of the structural damping ratio was then added back to the aerodynamic damping ratio for each test condition to give the total damping ratio that is presented in the results.

The ratios of aerodynamic damping to critical damping obtained in this manner apply only to the particular mechanical systems used in these tests. In order to make the damping measurements of more general value, a nondimensional damping force coefficient C_h can be defined in terms

of the usual flutter parameters, reduced frequency and mass ratio, in such a manner as to permit estimation of aerodynamic damping of similar configurations having somewhat different structural characteristics. As indicated in appendix B (eq. B5)

$$\frac{C_A}{C_{cr}} = \frac{\pi\rho V r^2}{2M_s\lambda}\int_0^{L/r} C_{N,\alpha}\left[\frac{R\left(\frac{x}{r}\right)}{r}\right]H^2\left(\frac{x}{r}\right)d\left(\frac{x}{r}\right)$$

and $C_h^{\bullet}$ is defined by

$$\frac{C_A}{C_{cr}} = \frac{\pi\rho V r^2}{2M_s\lambda}C_h^{\bullet}$$

or, if this expression is rewritten in terms of conventional flutter parameters,

$$C_h^{\bullet} = 2k\mu\frac{C_A}{C_{cr}}$$

where

k reduced frequency, $\frac{\lambda L}{V}$

λ an effective mass ratio, $\frac{M_s}{\pi r^2\rho L}$

V flow velocity

r radius of cylindrical portion of model

ρ mass density of test medium

L overall length of configuration

M_s generalized mass of configuration in vibration mode of interest

λ frequency of vibration in mode of interest

This damping-force coefficient $C_h^{\bullet}$ is useful in scaling model results to equivalent full-scale conditions and is used in the presentation of the results of the investigation along with the damping ratio $\frac{C_A}{C_{cr}}$.

RESULTS AND DISCUSSION

The values of damping observed in this investigation for the various test conditions are shown in figures 8 to 11. Shown in figure 8(a) is the variation of the ratio of total damping to critical damping with the flow parameter ρV (test-section air density multiplied by the free-stream velocity) for model configuration 1 oscillating in the first free-free mode at several Mach numbers. The parameter ρV is used because the theories applied have all predicted a linear variation of aerodynamic damping with ρV for a given Mach number. (See appendix B.) The dashed line is the averaged structural damping ratio. Shown plotted are data obtained from the power input method (open symbols) and from freely decaying oscillations (solid symbols). The freely decaying oscillations data is an average of that obtained from the electronic dampometer and from the oscillograph records. It should be mentioned that the free-decay method could not be used transonically because of the very uneven decays caused by the model response to the transonic flow conditions. Although there is scatter in the data, some observations can be made. First, note that the aerodynamic damping ratio is small, being on the order of 60 percent of the structural damping ratio at the maximum ρV tested.

Also, note that for the supersonic Mach numbers investigated in the Langley Unitary Plan wind tunnel, the ratio of aerodynamic damping to critical damping appears to vary linearly with ρV whereas in general this is not true for the transonic Mach numbers.

In figure 8(b) the aerodynamic derivative $C_{h}^{\cdot}$ for the first free-free vibration mode of model configuration 1 is plotted against Mach number for several of the higher values of ρV. Data from both the power-input and free-decay methods of measurement are included for the Mach number range from 1.76 to 2.87. Within the scatter of the data (which is greatly magnified on the basis of the parameter $C_{h}^{\cdot}$), there is apparently little Mach number effect. Also shown in figure 8(b) are some aerodynamic damping derivatives calculated (using experimentally determined mode shapes) from piston theory, momentum theory, second-order shock-expansion theory, second-order Van Dyke theory, and a theory by Bond and Packard. (See appendix B for an explanation of how these various theories were applied.) The second-order shock-expansion and second-order Van Dyke theories show the worst agreement with experiment. The trend with Mach number indicated by piston theory is not evident in the experimental results. The Bond-Packard theory agrees very well with the experimental results.

The results of damping measurements in the second free-free vibration mode of model configuration 1 are shown in figure 9. The variation of total damping with the flow parameter ρV at several Mach numbers is

shown in figure 9(a). Note that, unlike the first-mode data, the structural damping as determined from the power input and free-decay methods is not the same. The reason for this wide disparity has not been resolved and warrants further investigation. It is felt, however, that under forced vibration conditions the model may be responding in a mode that degenerates into a slightly different shape when the model is freely decaying. If this is the case, the change is not significant enough to alter the trend reflected in the aerodynamic damping shown for the two methods in figure 9(a). Although the structural damping differs almost by a factor of two, the aerodynamic damping measured by the two methods is in fairly good agreement. In both cases, the maximum aerodynamic damping is less than 40 percent of the corresponding structural damping.

In figure 9(b), the damping derivative $C_{h}^{\cdot}$ for the second free-free mode is plotted against Mach number for several of the higher values of ρV. Experimental values determined from the two methods are shown with some calculated derivatives. No Mach number effect is apparent from the power-input data although the free-decay-method data show an apparent decrease in the damping derivative with Mach number over the range that the method was usable. The same trend is seen to be predicted by the data calculated by using the piston theory. The other theories are not in good agreement with the experimental values.

The results of damping measurements on the first free-free mode of model configuration 2 (which had a frequency about twice that of configuration 1) is shown in figure 10. The variation of total damping ratio with the flow parameter ρV is shown in figure 10(a) for several Mach numbers. The primary observation to be made here is that the maximum aerodynamic damping is about 60 percent of the structural damping, which is about the same as it was for configuration 1. Also, the values of $C_{h}^{\cdot}$ for the two configurations are roughly the same at comparable Mach numbers. The results of tests on the two configurations therefore indicate little, if any, reduced-frequency effect for the range investigated.

In figure 10(b) the variation of the aerodynamic damping derivative $C_{h}^{\cdot}$ with Mach number is shown for several values of ρV. No Mach number effect is apparent in the experimental data. Also shown are values of $C_{h}^{\cdot}$ obtained from quasi-steady calculations based on static pressure-distribution measurements made on a rigid model of like geometry given in reference 9. These calculated values are seen to be low with respect to the experimental damping derivatives as was the case for the purely theoretical approaches used on configuration 1.

Figure 11 presents the variation of total damping with Mach number for model configuration 3 vibrating in the first free-free bending mode. The interesting point to be observed here is that the addition of the

"hammerhead" nose to configuration 1 resulted in small negative aerodynamic damping over a portion of the Mach number range from about 0.95 to 1.00.

It might be mentioned that the scarcity of data points for this configuration relative to the other configurations tested is due to the fact that the model response to buffeting loads was so severe that the springs that supported the model on the sting kept breaking before the data could be obtained.

A few remarks on the results of the test program in general are in order. Although an attempt was made to measure aerodynamic stiffness in addition to aerodynamic damping in the elastic modes, no discernible change in model frequency was apparent outside the normal scatter in the data between the wind-off and the various tunnel wind-on conditions. (Wind-on frequency determination was accurate only to approximately 1 percent.) Likewise, attempts to measure aerodynamic damping in the third free-free mode proved to be futile because of the apparently extremely low values even under maximum ρV conditions. Also, "hoop" modes appearing in the third free-free bending mode made accurate determination of the mode shape extremely difficult.

CONCLUDING REMARKS

Aerodynamic damping measurements made on a sting-mounted aeroelastic model with a blunted conical nose and a cylindrical afterbody over a Mach number range from 0.8 to 2.87, and on a model with a "hammerhead" nose at Mach numbers from 0.9 to 1.2 indicate that the aerodynamic damping in the elastic modes of vibration was small for all configurations tested. The maximum aerodynamic damping measured was approximately 60 percent of the structural damping. The aerodynamic damping was found to be even less for vibration modes higher than the first.

Reduced-frequency effects were found to be negligible for the range investigated.

Of the various theoretical methods considered, only the Bond-Packard theory for damping in the first elastic mode showed good agreement with the experimental results. Generally, the experimentally determined derivatives were larger than those predicted by the various theories used.

Measurements made on the configuration that had a hammerhead nose indicated small negative aerodynamic damping in the Mach number range from 0.95 to 1.0.

Aerodynamic stiffness effects were found to be small and fell within the experimental scatter since wind-on frequency determination was accurate only to approximately 1 percent.

Langley Research Center,
National Aeronautics and Space Administration,
Langley Station, Hampton, Va., June 7, 1962.

APPENDIX A

DEVELOPMENT OF DATA-REDUCTION RELATIONS FOR FORCED OSCILLATION DAMPING MEASUREMENT TECHNIQUE

The purpose of this appendix is to present in some detail the relationships necessary to the data reduction for the forced-oscillation damping-measurement technique. It should be pointed out that a somewhat similar presentation is given in reference 10 for a cantilever wing oscillating in the first bending mode.

The system considered here is a flexible beam having running mass $m(x)$ and stiffness $EI(x)$ which is attached to two soft linear springs k_1 and k_2 at longitudinal coordinates x_1 and x_2. The system is excited by a sinusoidal force $F(t)$ applied perpendicular to the beam center line at longitudinal station x_3. In addition to the force $F(t)$ and the inertia and spring force loading due to the motion of the beam, the beam is subjected to a running aerodynamic shear loading $W(x,t)$. The system is presented schematically in sketch 1. The x,y coordinate system is fixed relative to the undisturbed beam.

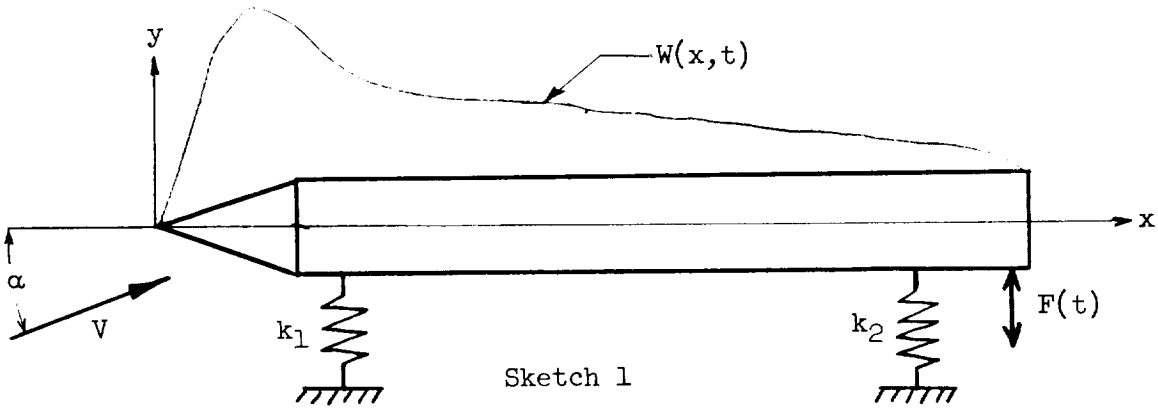

Sketch 1

In the absence of the driving force $F(t)$ and the aerodynamic loading $W(x,t)$ the differential equation which defines the transverse bending free-vibration characteristics for the undamped system is

$$\frac{\partial^2}{\partial x^2}EI(x)\frac{\partial^2 y(x,t)}{\partial x^2} + k_1\, y(x,t)\, \delta(x-x_1) + k_2\, y(x,t)\, \delta(x-x_2) = -m(x)\frac{\partial^2 y(x,t)}{\partial t^2} \tag{A1}$$

where the function $\delta(x-x_n)$ is a Dirac function with the property that

$$\int_0^L y(x,t)\ \delta(x-x_n)\ dx = y(x_n,t) \tag{A2}$$

The displacement function $y(x,t)$ may be expanded into a series of products of time and space functions.

$$y(x,t) = \sum_{m=1}^{\infty} a_m(t)\ h_m(x) \tag{A3}$$

By choosing the normal modal functions of the system defined by equation (A1) for the space functions $h_m(x)$ and applying a Galerkin procedure along with the appropriate orthogonality conditions, equation (A1) becomes a set of equations:

$$M_{s,m}\ddot{a}_m(t) + \omega_m^2 M_{s,m} a_m(t) = 0 \qquad (m = 1, 2, 3, \ldots) \tag{A4}$$

where the generalized mass $M_{s,m}$ is $\int_0^L m(x)\ h_m^2(x)\ dx$ and ω_m is the natural frequency of vibration of the mth mode of the system defined by equation (A1). A viscous-type structural damping may be included by adding a term $B_m\dot{a}_m(t)$.

$$M_{s,m}\ddot{a}_m(t) + B_m\dot{a}_m(t) + \omega_m^2 M_m a_m(t) = 0 \qquad (m = 1, 2, 3, \ldots) \tag{A5}$$

Now with the sinusoidal force $F(t) = F_0 e^{i\omega t}$ applied to the damped system at the point $x = x_3$, the set of equations of motion is

$$M_{s,m}\ddot{a}_m(t) + B_m\dot{a}_m(t) + \omega_m^2 M_{s,m} a_m(t) = \int_0^L F(t)\ h_m(x)\ \delta(x-x_3)\ dx$$

$$= F(t)\ h_m(x_3) \qquad (m = 1, 2, 3, \ldots) \tag{A6}$$

The deflection shape assumed by the beam after all transient motion has subsided is

$$y(x,t) = \sum_{m=1}^{\infty} \frac{F(t)\, h_m(x_3)\, h_m(x)}{(\omega_m^2 - \omega^2)M_{s,m} + iB_m} \tag{A7}$$

If the displacement function $y(x,t)$ were plotted against ω, there would be n peaks associated with $\omega = \Omega_n$. Each of these peaks would have a shape very similar to that found for a lightly damped mass oscillator. For reasonably well separated frequencies ω_m,

$$\Omega_n \approx \omega_m \tag{A8}$$

Associated with each of these resonance frequencies Ω_n, there will be a particular deflection shape. The shapes are given by equation (A7) when $\omega = \Omega_n$. The function $y_n(x,t)$ may be separated into the product of a time and space function

$$y_n(x,t) = b_n(t)\, H_n(x) \tag{A9}$$

The function $H_n(x)$ may be thought of as a coupled-mode shape and the frequency Ω_n as the corresponding coupled-mode frequency. These modes are coupled as a result of the damping forces and the shaker forces. Because the structural damping is small, the coupled- and uncoupled-mode shapes and frequencies are almost identical. These shapes and frequencies may be calculated or measured experimentally. The latter method was chosen for this investigation.

In this development the motion of the system will be examined only at these coupled-mode resonance peaks. At the nth resonance condition the potential energy of the system is $\frac{1}{2}K_n b_n(t)^2$ where K_n may be thought of as a generalized stiffness and is equal to

$$\int_0^L EI(x)\left[\frac{\partial^2}{\partial x^2}H_n(x)\right]^2 dx + k_1 H_n(x_1)^2 + k_2 H_n(x_2)^2$$

The kinetic energy of the system is $\frac{1}{2}M_{s,n}\dot{b}_n(t)^2$ where $M_{s,n}$ is a generalized mass and is equal to

$$\int_0^L m(x)\ H_n^2(x)\ dx$$

The dissipation function associated with the assumption of viscous structural damping is $\frac{1}{2}C_{s,n}\dot{b}_n(t)^2$ where $C_{s,n}$ is the generalized damping and is equal to

$$\int_0^L c_{s,n}\ H_n^2(x)\ dx$$

The virtual work associated with the external loads $F(t)$ and $W(x,t)$ acting on the system through a virtual displacement $\delta b_n(t)\ H_n(x_3)$ is

$$\delta b_n(t)\ F(t)\ H_n(x_3) + \delta W_A \qquad (A10)$$

Before the virtual work done by the aerodynamic forces can be expressed more precisely than by δW_A, the nature of $W(x,t)$ must be examined in some detail. This loading may be separated into three categories.

The first is that due to the mean angle of attack α. Since this portion of the aerodynamic loading is steady state and produces only static deflections of the structure, it will not be treated further.

The second is of a random type being produced by turbulence, separated flow, and so forth. These random forces will produce random deflections $b_{n,r}(t)$, velocities $\dot{b}_{n,r}(t)$, and accelerations $\ddot{b}_{n,r}(t)$ of the beam. The virtual work done by the random aerodynamic loading is

$$\delta b_n(t) \int_0^L W_r(x,t)\ H_n(x)\ dx$$

where $W_r(x,t)$ is the random aerodynamic running shear load.

The third type of aerodynamic loading is that due to the motion of the beam itself. This portion of the aerodynamic loading may be separated into three parts: inertia, damping, and spring forces. It must be assumed that the aerodynamic inertia and spring forces are reasonably small relative to their structural counterparts, so that the mode shapes will not differ appreciably from those measured with zero wind. The virtual work done by these three aerodynamic forces is

$$-\delta b_n(t)\,\ddot{b}_n(t)\int_0^L A_{I,n}\,H_n(x)\,dx - \delta b_n\,\dot{b}_n(t)\int_0^L A_{c,n}\,H_n(x)\,dx$$

$$-\delta b_n(t)\,b_n(t)\int_0^L A_{K,n}\,H_n(x)\,dx$$

where $A_{I,n}$, $A_{c,n}$, and $A_{K,n}$ are distribution functions of the inertial, damping, and stiffness components of the aerodynamic loading.

Combining these expressions the total aerodynamic virtual work is

$$\delta W_A = -\delta b_n(t)\left[M_{A,n}\,\ddot{b}_n(t) + C_{A,n}\,\dot{b}_n(t) + K_{A,n}\,b_n(t) - F_{r,n}\right] \qquad \text{(All)}$$

where

$$M_{A,n} = \int_0^L A_{I,n}\,H_n(x)\,dx$$

$$C_{A,n} = \int_0^L A_{c,n}\,H_n(x)\,dx$$

$$K_{A,n} = \int_0^L A_{K,n}\,H_n(x)\,dx$$

$$F_{r,n} = \int_0^L W_r(x,t)\,H_n(x)\,dx$$

By applying Lagrange's dynamical equation of motion, the differential equation of motion of the system under the applied shaker and aerodynamic loading is

$$\left(M_{s,n} + M_{A,n}\right)\left[\ddot{b}_n(t) + \ddot{b}_{n,r}(t)\right] + \left(C_{s,n} + C_{A,n}\right)\left[\dot{b}_n(t) + \dot{b}_{n,r}(t)\right]$$

$$+ \left(K_{s,n} + K_{A,n}\right)\left[b_n(t) + b_{n,r}(t)\right] = F(t)\, H_n(x_3) + F_{r,n} \qquad (A12)$$

Multiplying equation (A12) by $F(t)$ and taking time averages yields

$$\left(M_{s,n} + M_{A,n}\right)\overline{\ddot{b}_n(t)\, F(t)} + \left(M_{s,n} + M_{A,n}\right)\overline{\ddot{b}_{n,r}(t)\, F(t)}$$

$$+ \left(C_{s,n} + C_{A,n}\right)\overline{\dot{b}_n(t)\, F(t)} + \left(C_{s,n} + C_{A,n}\right)\overline{\dot{b}_{n,r}(t)\, F(t)}$$

$$+ \left(K_{s,n} + K_{A,n}\right)\overline{b_n(t)\, F(t)} + \left(K_{s,n} + K_{A,n}\right)\overline{b_{n,r}(t)\, F(t)}$$

$$= H_n(x_3)\,\overline{F(t)^2} + \overline{F_{r,n}\, F(t)} \qquad (A13)$$

where the bars indicate a time average over a period of time T. However, as T approaches ∞, the products

$$\left(M_{s,n} + M_{A,n}\right)\overline{\ddot{b}_{n,r}(t)\, F(t)}$$

$$\left(C_{s,n} + C_{A,n}\right)\overline{\dot{b}_{n,r}(t)\, F(t)}$$

$$\left(K_{s,n} + K_{A,n}\right)\overline{b_{n,r}(t)\, F(t)}$$

$$\overline{F_{r,n}\, F(t)}$$

vanish since there is no correlation between the random part of the response and the sinusoidal forcing function and thus the time average

of the product of these quantities is zero. Also, since the system is being forced at resonance, the force is in phase with $\dot{b}_n$ and is 90° out of phase with b_n and $\ddot{b}_n$; therefore the products

$$\left(M_{s,n} + M_{A,n}\right)\overline{\ddot{b}_n(t)\ F(t)} = \left(K_{s,n} + K_{A,n}\right)\overline{b_n(t)\ F(t)} = 0 \tag{A14}$$

Consequently,

$$\left(C_{s,n} + C_{A,n}\right)\overline{\dot{b}_n(t)\ F(t)} = H_n\left(x_3\right)\ \overline{F(t)^2} \tag{A15}$$

or

$$C_{s,n} + C_{A,n} = \frac{H_n\left(x_3\right)\ \overline{F(t)^2}}{\overline{\dot{b}_n(t)\ F(t)}} \tag{A16}$$

The critical damping of the system is defined as

$$C_{cr,n} = 2\sqrt{\left(M_{s,n} + M_{A,n}\right)\left(K_{s,n} + K_{A,n}\right)} = 2\lambda_n\left(M_{s,n} + M_{A,n}\right) \tag{A17}$$

However, since $M_{A,n}$ is small relative to $M_{s,n}$, the critical damping is

$$C_{cr,n} = 2\lambda_n M_{s,n} \tag{A18}$$

The frequency λ_n is the frequency of the system in the nth mode with the external aerodynamic loading present. The ratio of total damping to the critical damping is

$$\frac{C_{A,n} + C_{s,n}}{C_{cr,n}} = \frac{H_n\left(x_3\right)\ \overline{F(t)^2}}{\overline{\dot{b}_n(t)\ F(t)}\ 2M_{s,n}\ \lambda_n} \tag{A19}$$

If the sinusoidal force $F(t)$ is applied by an electromagnetic shaker, it can be shown that the current passing through the shaker moving coil is proportional to the output force of the shaker.

$$F(t) = q_1 I \tag{A20}$$

Also, the quantity $\overline{\dot{b}_n(t)\, F(t)}$ is proportional to the power consumed by the shaker moving coil less any power losses due to coil resistance.

$$\overline{\dot{b}_n(t)\, F(t)} = q_{2,n}\left(P - I^2R\right) \tag{A21}$$

Therefore, by using the relationship given by equation (A20), the expression for the damping ratio becomes

$$\frac{C_{A,n} + C_{s,n}}{C_{cr,n}} = \frac{q_1^2\, H_n\left(x_3\right)\, I^2}{q_{2,n}\left(P - I^2R\right)\left(2M_{s,n}\, \lambda_n\right)} \tag{A22}$$

The aerodynamic damping ratio $\frac{C_{A,n}}{C_{cr,n}}$ is determined by measuring the structural damping ratio $\frac{C_{s,n}}{C_{cr,n}}$ in still air before each test and subtracting it as a tare from the total damping measured during the test. It should be pointed out that external forces on the model can produce coil velocities which induce correlated voltages and currents in the electrical system. These currents are kept small, however, by driving the shaker coil with a voltage generator that has an impedance which is high with respect to that of the moving coil.

APPENDIX B

CALCULATED AERODYNAMIC DAMPING COEFFICIENTS

The theoretical model used here is a slender cone cylinder oscillating harmonically about a mean angle of attack of 0° in its nth transverse bending mode at frequency λ_n and with tip amplitude $b_n(t)$ and normalized mode shape $H_n(x)$. The theoretical model differs from the experimental one in that the conical nose section is assumed to be sharp. Since only the aerodynamic damping is desired, only those forces generated by the vertical velocity $\dot{b}_n(t)\ H_n(x)$ are considered.

The generalized force associated with the aerodynamic damping is

$$Q_{\dot{h},n} = \dot{b}_n(t) \int_0^L A_{c,n}\ H_n(x)\ dx \tag{B1}$$

where A_c is the distribution of the aerodynamic damping forces per unit length. The subscript n will be omitted hereafter since reference is made only to a system oscillating in a single mode.

Using a quasi-steady approach the distribution function A_c may be expressed as

$$A_c = 2q\pi R(x)\ C_{N,\alpha}\ \frac{H(x)}{V} \tag{B2}$$

where $R(x)$ is the function which describes the shape of the body, $C_{N,\alpha}$ is the section steady-state normal-force coefficient slope, and $\frac{H(x)}{V}$ is a normalized angle of attack. Equation (B1) may now be written

$$Q_{\dot{h}} = \left[\pi\rho V \int_0^L C_{N,\alpha}\ R(x)\ H^2(x)\ dx\right] \dot{b}(t) \tag{B3}$$

where the term in the brackets is C_A.

$$C_A = \pi\rho V \int_0^L C_{N,\alpha}\, R(x)\, H^2(x)\, dx \tag{B4}$$

or, in nondimensional form,

$$\frac{C_A}{C_{cr}} = \frac{\pi\rho V r^2}{2M_s\lambda} \int_0^{\frac{L}{r}} C_{N,\alpha}\left[\frac{R\left(\frac{x}{r}\right)}{r}\right] H^2\left(\frac{x}{r}\right)\, d\left(\frac{x}{r}\right) \tag{B5}$$

The theories of references 2 to 4 are readily adaptable to the quasi-steady approach. In general, the equation for the aerodynamic damping coefficient (B4) will have to be integrated in two parts - one part for the conical nose portion and one for the cylindrical afterbody. The expressions for the section normal-force coefficient as predicted by the methods presented in references 2 to 4 are presented in the following table:

Theory	Reference	$C_{N,\alpha}$ for the -	
		Conical nose	Afterbody
Second-order Van Dyke	2	$2\tan\theta\left\{1 - \tan^2\theta\left[M_\infty^2 \log_e\left(\frac{2}{\sqrt{M_\infty^2 - 1}\tan\theta}\right) - \frac{3}{2}M_\infty^2 + 1\right]\right\}$	0
Second-order piston	3	$\frac{1}{M_\infty} + \left(\frac{\gamma+1}{2}\right)\tan\theta + \left(\frac{\gamma+1}{4}\right)M_\infty \tan^2\theta$	$\frac{1}{M_\infty}$
Second-order shock expansion	4	Exact solution for cone (ref. 5)	$\frac{1}{4}G_1 G_2 e^{-G_2 \frac{X}{2r}}$

The functions G_1 and G_2 are functions of M_∞ and θ alone and X is a distance downstream from the cone-cylinder intersection. (See appendix C of ref. 4.)

Another theory which lends itself readily to aerodynamic damping calculations is the linear small-aspect-ratio unsteady-flow theory given in reference 6. This theory gives for A_c

$$A_c = \pi\rho V\left[2R(x)^2 \frac{d}{dx}H(x) + 2R(x)\frac{d}{dx}R(x)\, H(x)\right] \tag{B6}$$

The aerodynamic damping coefficient is

$$C_A = \pi\rho V \int_0^L \frac{d}{dx}\left[R^2(x)\ H(x)^2\right]dx \tag{B7}$$

Performing the integration in equation (B7) yields a very concise expression for the aerodynamic damping

$$C_A = \pi\rho V r^2 H(L)^2 \tag{B8}$$

where $H(L)$ is the value of the normalized deflection shape at the rear of the model, and r is the radius of the cylindrical portion of the model.

In reference 7 Bond and Packard present an analysis based on a slender-body approximation, the solution of which is obtained in a definite integral that has not been found to be integrable in finite form. Evaluation of the integral has been accomplished by numerical methods, and the computation forms have been programed for the IBM 704 data processing machine for certain cases.

The analysis of reference 7 has been used by the Ames Research Center to calculate values of the damping force coefficient $C_{\dot{n}}$ for the first two flexible modes of model configuration 1 at supersonic Mach numbers.

The results of those calculations are presented in figures 8 and 9 along with the results of the other theoretical approaches used.

REFERENCES

1. Bratt, J. B.: Wind Tunnel Techniques for the Measurement of Oscillatory Derivatives. British A.R.C. 22,146, Aug. 19, 1960.

2. Van Dyke, Milton D.: A Study of Second-Order Supersonic Flow Theory. NACA Rep. 1081, 1952. (Supersedes NACA TN 2200.)

3. Miles, J. W., and Young, Dana: Generalized Missile Dynamics Analysis. III - Aerodynamics. GM-TR-0165-00360, Space Tech. Labs., The Ramo-Wooldridge Corp., Apr. 7, 1958.

4. Syvertson, Clarence A., and Dennis, David H.: A Second-Order Shock Expansion Method Applicable to Bodies of Revolution Near Zero Lift. NACA Rep. 1328, 1957. (Supersedes NACA TN 3527.)

5. Stone, A. H.: On Supersonic Flow Past a Slightly Yawing Cone. Jour. Math. and Phys., vol. XXVII, no. 1, Apr. 1948, pp. 67-81.

6. Garrick, I. E.: Some Research on High Speed Flutter. Third Anglo-American Aero. Conf., Sept. 4-7, 1951 (Brighton, England). R.A.S., 1952, pp. 419-446J.

7. Bond, Reuben, and Packard, Barbara B.: Unsteady Aerodynamic Forces on a Slender Body of Revolution in Supersonic Flow. NASA TN D-859, 1961.

8. Olsson, Carl Olof, and Orlik-Rückemann, Kazimierz: An Electronic Apparatus for Automatic Recording of the Logarithmic Decrement and Frequency of Oscillations in the Audio and Subaudio Frequency Range. Rep. No. 52, Aero. Res. Inst. of Sweden (Stockholm), 1954.

9. Coe, Charles F.: Steady and Fluctuating Pressures at Transonic Speeds on Two Space-Vehicle Payload Shapes. NASA TM X-503, 1961.

10. Rainey, A. Gerald: Measurement of Aerodynamic Forces for Various Mean Angles of Attack on an Airfoil Oscillating in Pitch and on Two Finite-Span Wings Oscillating in Bending With Emphasis on Damping in the Stall. NACA Rep. 1305, 1957. (Supersedes NACA TN 3643.)

TABLE I.- EXPERIMENTALLY DETERMINED NATURAL MODE SHAPES OF MODEL CONFIGURATIONS TESTED (NORMALIZED ON NOSE OF CONFIGURATIONS 1 AND 2)

x/L	Normalized deflections			
	Configuration 1		Configuration 2, mode 1	Configuration 3, mode 1
	Mode 1	Mode 2		
-0.019	-----	-----	-----	1.091
0	1.000	1.000	1.000	1.000
.10	.620	.462	.564	.577
.20	.235	-.095	.125	.155
.25	.050	-.306	-.095	-.055
.30	-.125	-.451	-.303	-.231
.35	-.273	-.494	-.472	-.368
.40	-.385	-.417	-.596	-.461
.50	-.478	-.073	-.712	-.538
.60	-.410	.335	-.644	-.447
.65	-.316	.450	-.553	-.338
.70	-.197	.476	-.417	-.184
.75	-.038	.388	-.239	0
.80	.133	.225	-.018	.195
.85	.320	.002	.209	.398
.90	.517	-.263	.438	.606
1.00	.930	-.950	.895	1.049

TABLE II.- PHYSICAL PROPERTIES OF MODEL CONFIGURATIONS TESTED

Range of x/L	Mass per unit length, lb-sec^2/ft^2, for -		
	Configuration 1	Configuration 2	Configuration 3
-0.0183 to 0	------	------	0.0180
0 to .0136	0.0155	0.0155	.0414
.0136 to .0271	.0155	.0155	.0598
.0271 to .0550	.0155	.0155	.0348
.0550 to .0818	.0155	.0155	.0428
.0818 to .0958	.4385	.0953	.4700
.0958 to .1355	.0155	.0155	.0504
.1355 to .1542	.1650	.1650	.2000
.1542 to .1682	.8975	.1175	1.0362
.1682 to .1720	.0155	.0155	.1424
.1720 to .2172	.0155	.0155	.0453
.2172 to .2312	.7485	.0795	.7761
.2312 to .2579	.0155	.0155	.0416
.2579 to .2748	.0155	.0155	.0296
.2748 to .3302	.0155	.0155	.0155
.3302 to .3442	.8375	.0995	.8375
.3442 to .4121	.0155	.0155	.0155
.4121 to .4291	.8695	.0595	.8695
.4291 to .5000	.0155	.0155	.0155
.5000 to .5140	.8735	.1335	.8735
.5140 to .5845	.0155	.0155	.0155
.5845 to .5985	.8725	.0605	.8725
.5985 to .6700	.0155	.0155	.0155
.6700 to .6870	.8125	.0995	.8125
.6870 to .7475	.0155	.0155	.0155
.7475 to .7620	.1247	.1247	.1247
.7620 to .7800	.6260	.0630	.6260
.7800 to .8460	.0155	.0155	.0155
.8460 to .8550	.0607	.0607	.0607
.8550 to .8870	.0155	.0155	.0155
.8870 to .9000	1.1275	.0595	1.1275
.9000 to .9460	.0155	.0155	.0155
.9460 to .9600	.2257	.2257	.2257
.9600 to 1.0000	.0155	.0155	.0155
Total weight, lb	19.68	4.76	21.29
Generalized mass, lb-sec^2/ft, mode 1	0.1081	0.0396	0.1269
Generalized mass, lb-sec^2/ft, mode 2	0.0740		
Natural frequency, cps, mode 1	85	159.0	79
Natural frequency, cps, mode 2	223		
Critical damping, lb-sec/ft, mode 1	115	79.2	126
Critical damping, lb-sec/ft, mode 2	208		

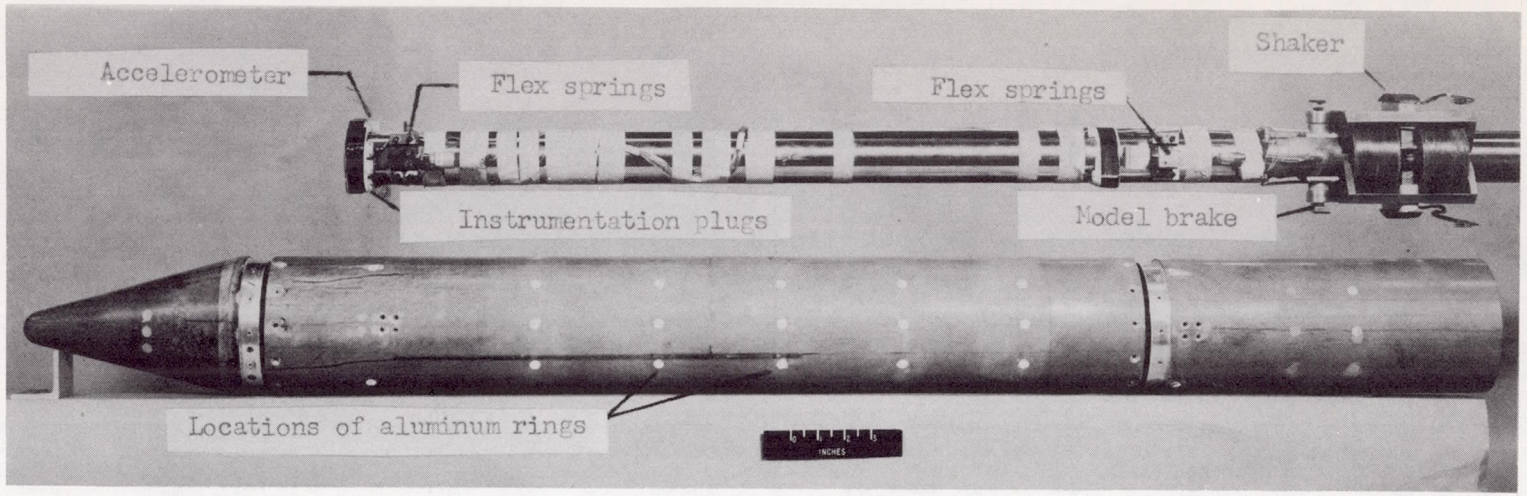

(a) General view of model and sting assembly. L-61-1191.1

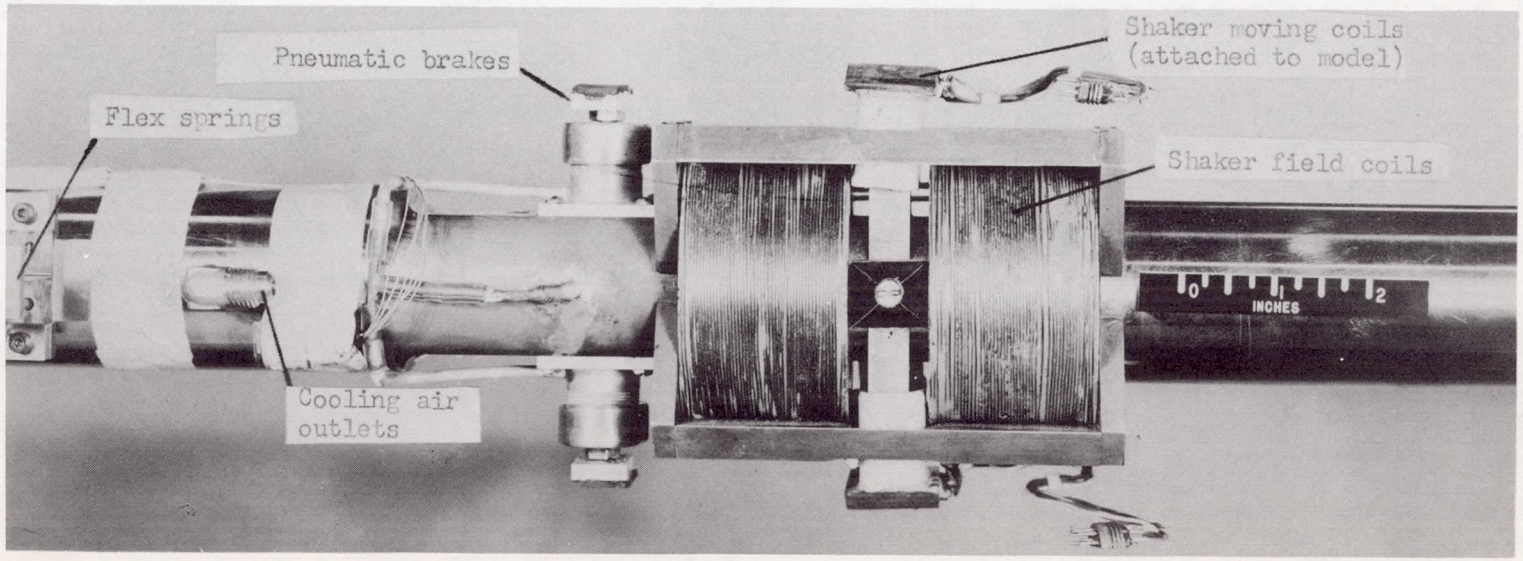

(b) Detailed view of sting in vicinity of shaker. L-61-1192.1

Figure 1.- Photograph of basic model and sting.

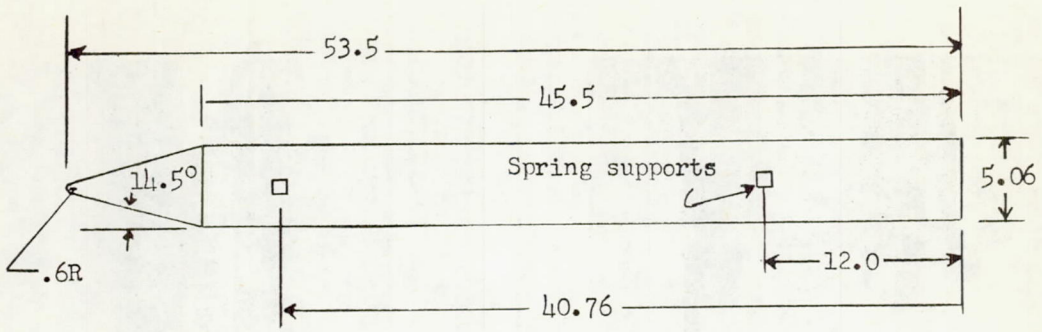

Configurations 1 and 2

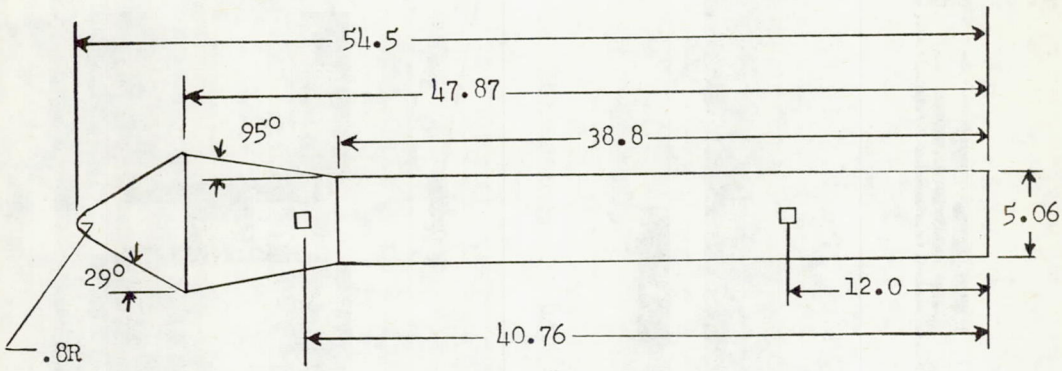

Configuration 3

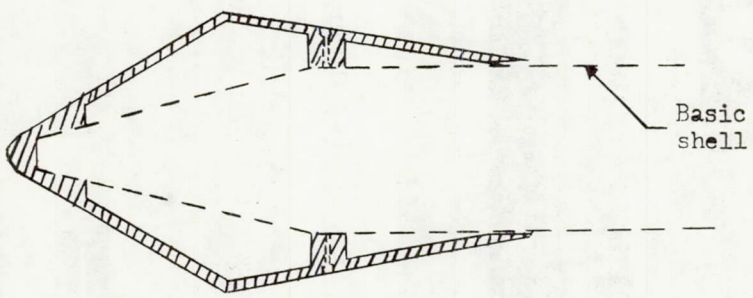

Longitudinal section through nose cap of configuration 3

Figure 2.- Geometry of configurations tested. All dimensions are in inches except as noted.

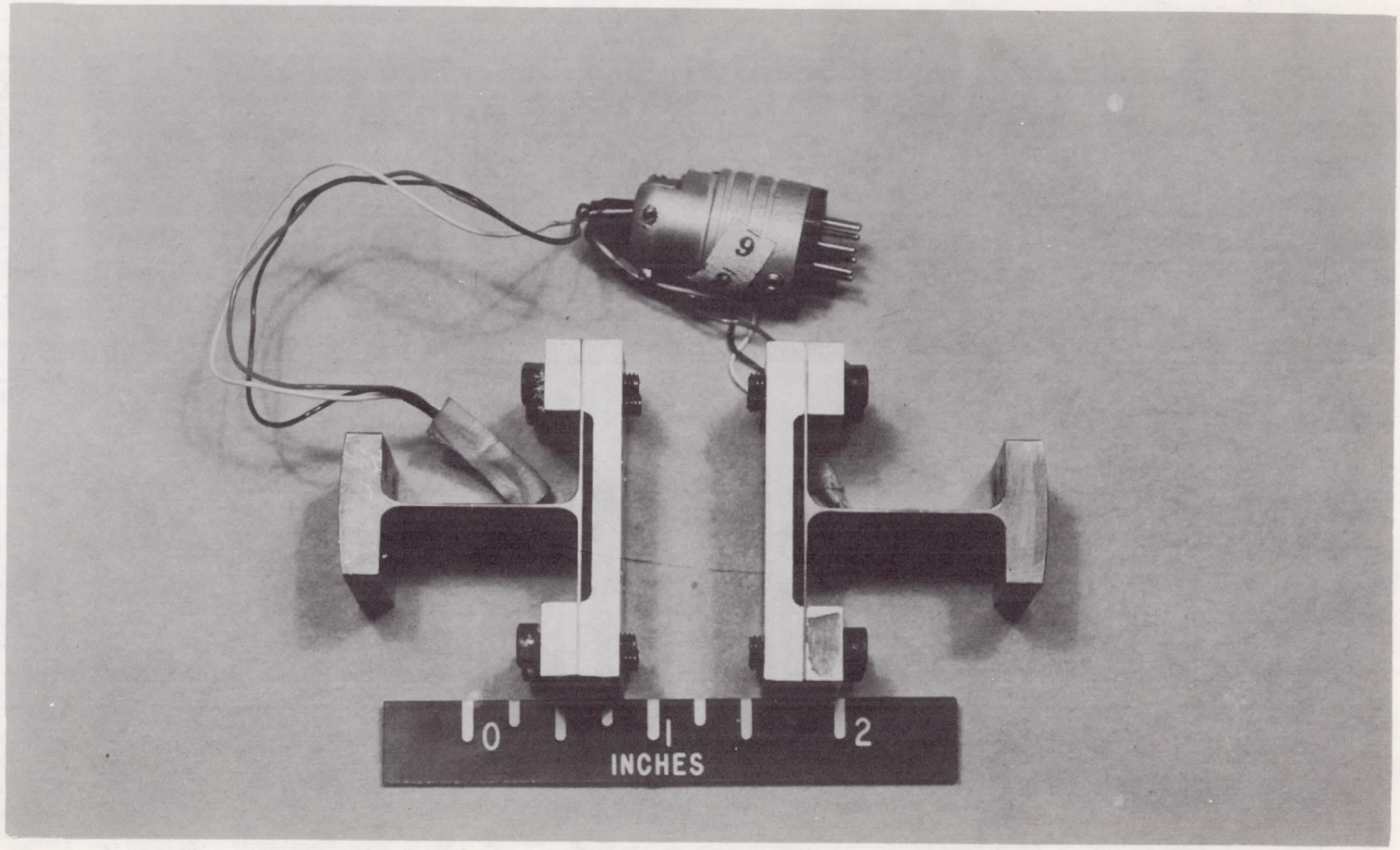

Figure 3.- Photograph of flex springs used to support model on sting. L-61-1193

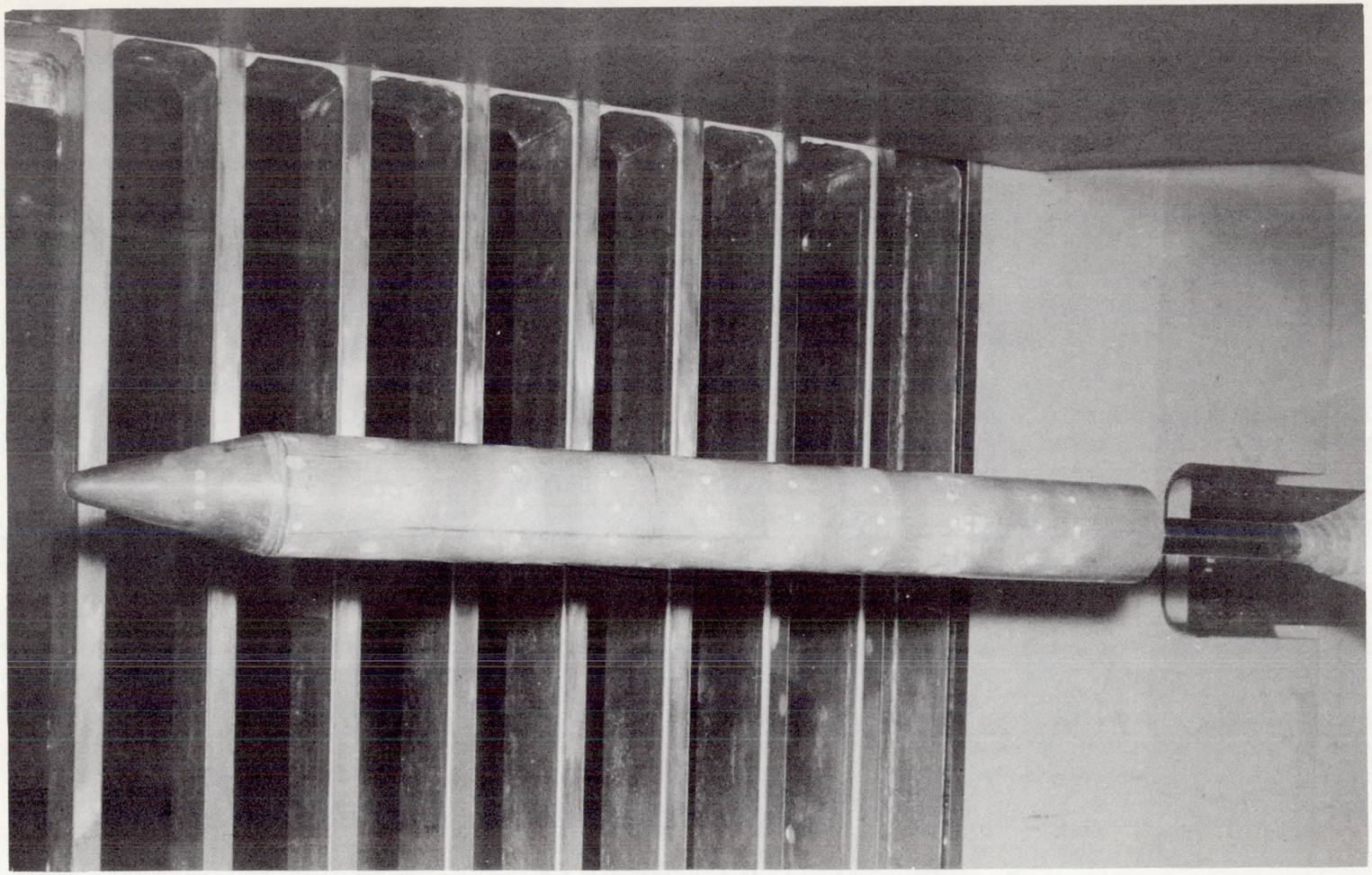

L-61-961

Figure 4.- Photograph of basic model mounted in Langley Unitary Plan wind tunnel.

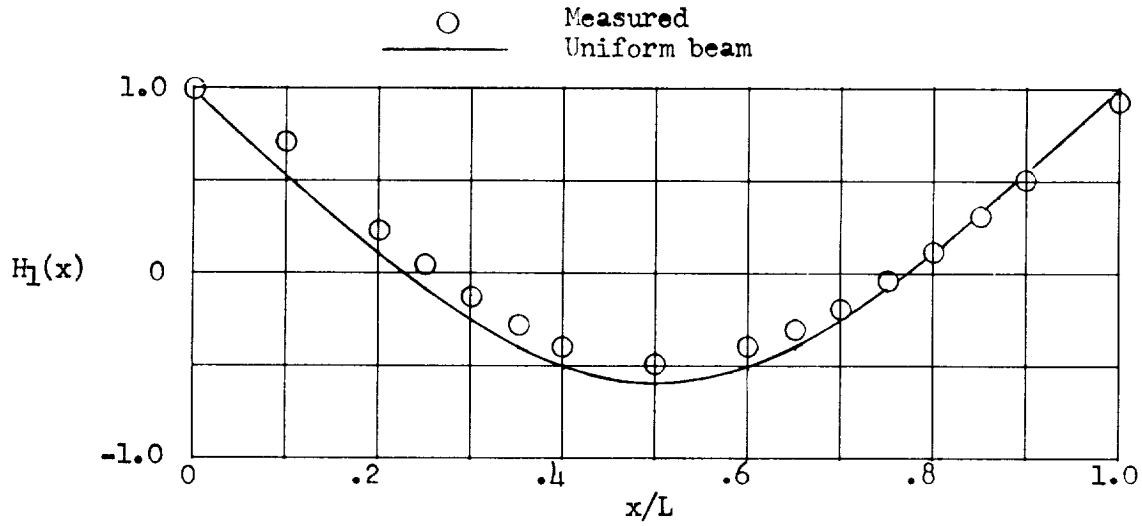

(a) Configuration 1; first mode; average C_s/C_{cr}, 0.0084; model frequency, 85 cps; uniform beam frequency, 84 cps.

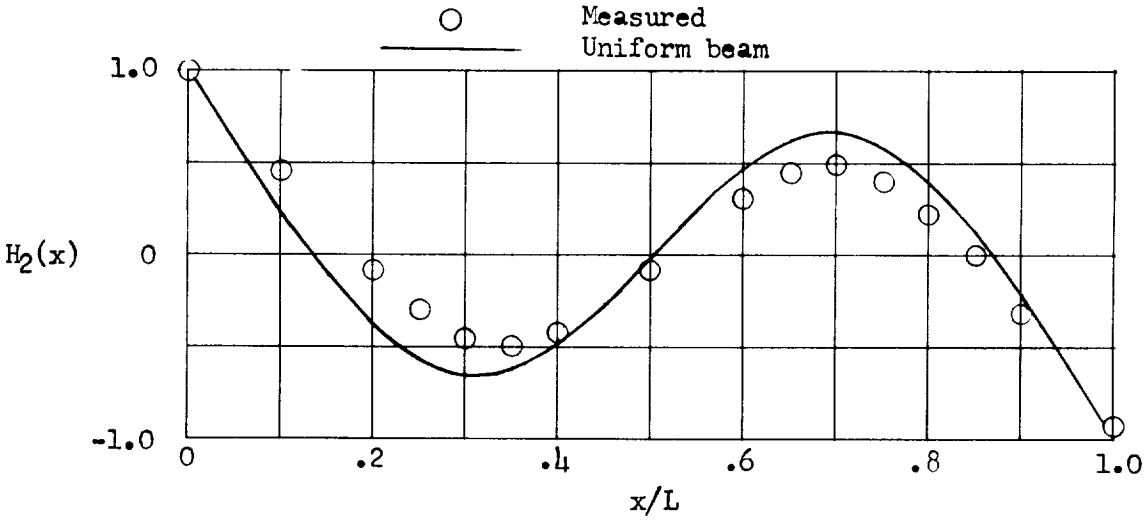

(b) Configuration 1; second mode; average C_s/C_{cr}, 0.011; model frequency, 223 cps; uniform beam frequency, 213 cps.

Figure 5.- Comparison of measured mode shapes with those of uniform free-free beam.

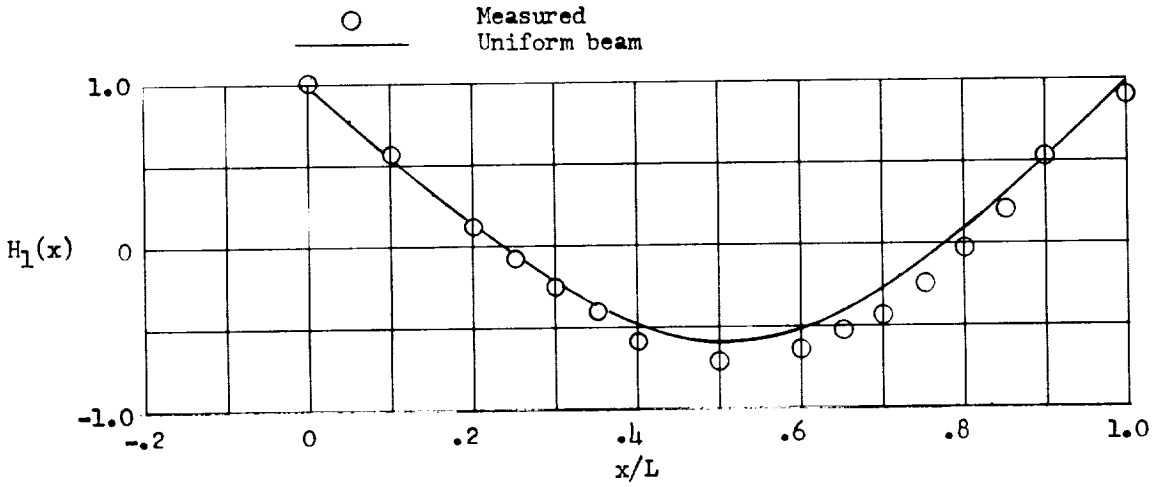

(c) Configuration 2; first mode; average C_s/C_{cr}, 0.0094; model frequency, 159 cps; uniform beam frequency, 171 cps.

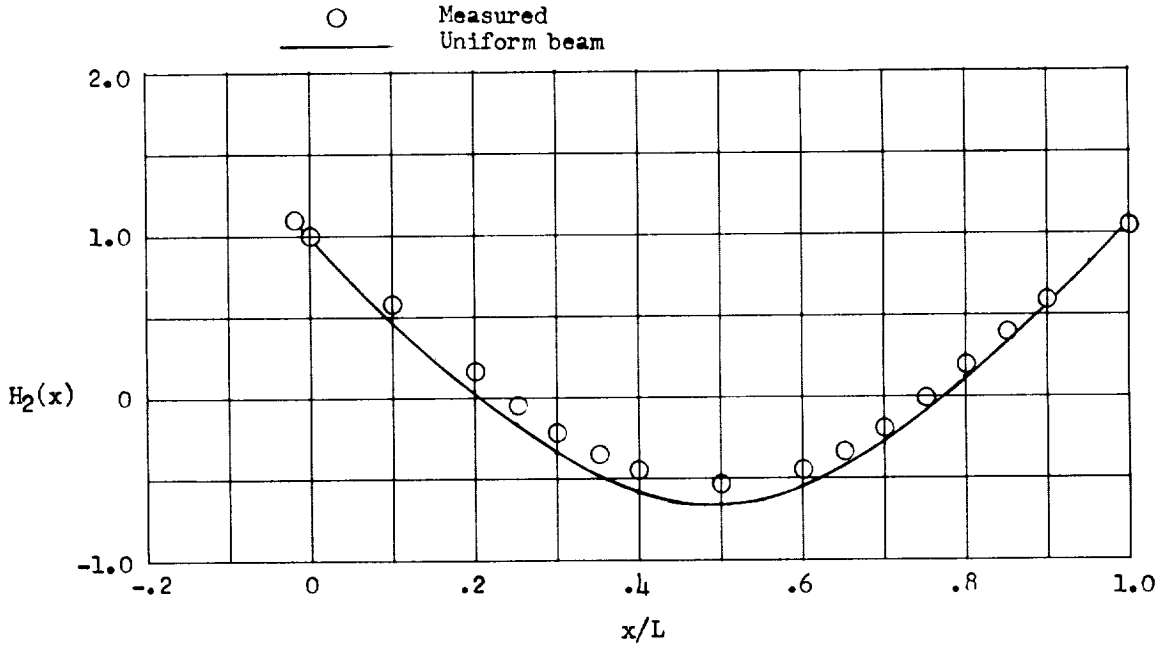

(d) Configuration 3; first mode; average C_s/C_{cr}, 0.0111; model frequency, 79 cps; uniform beam frequency, 81 cps.

Figure 5.- Concluded.

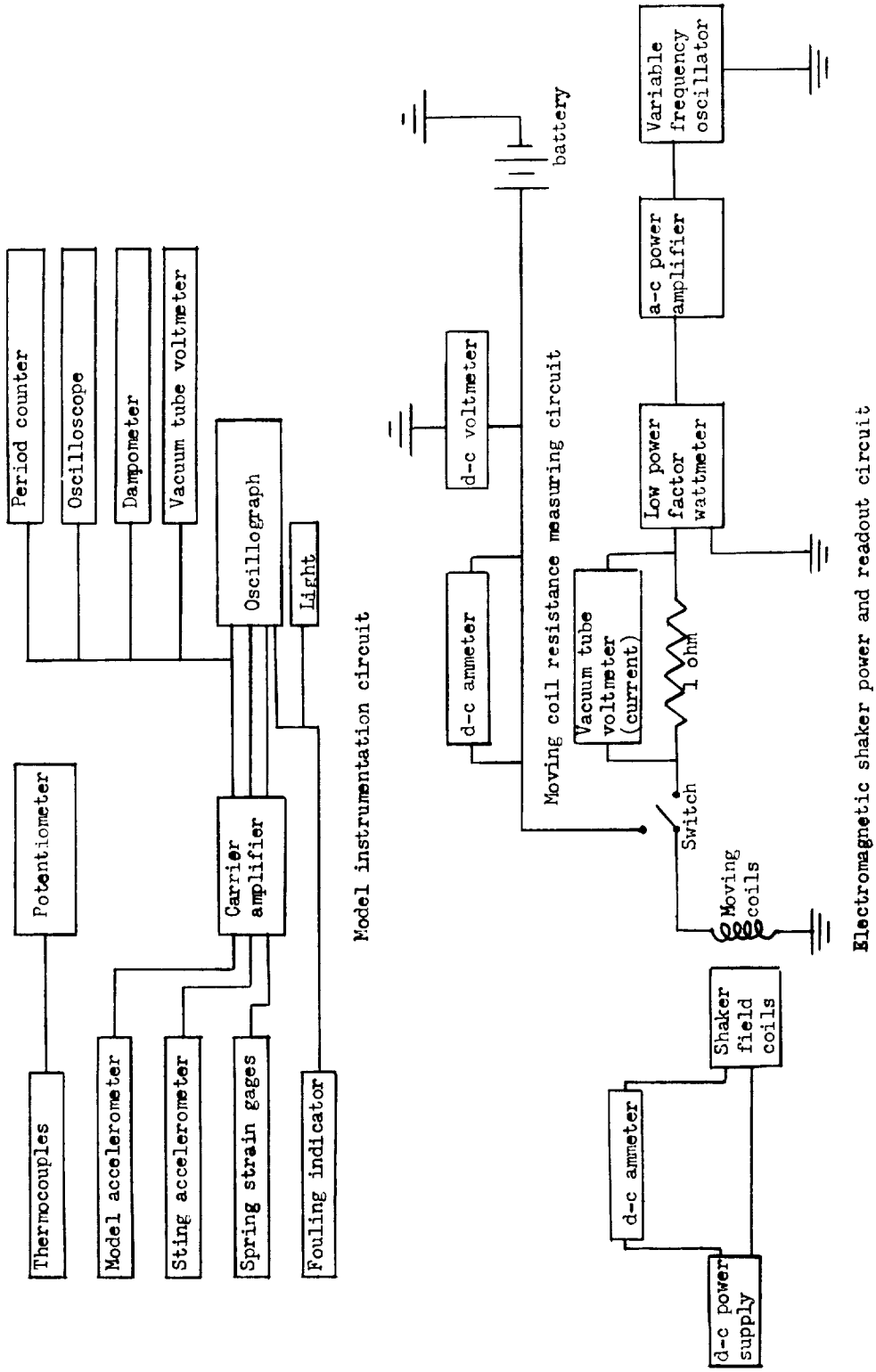

Figure 6.- Block diagram of model, shaker, and readout instrumentation.

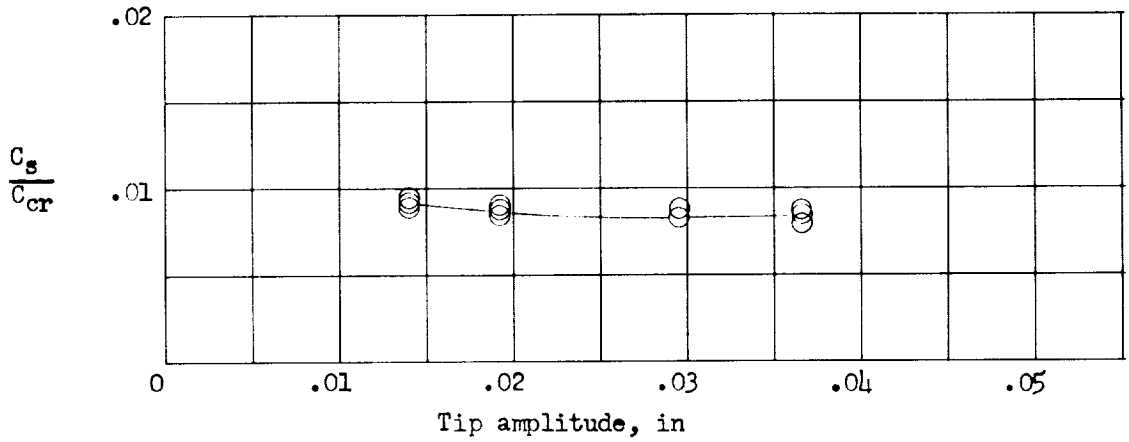

(a) Variation of structural damping coefficient with model amplitude for constant model skin temperature.

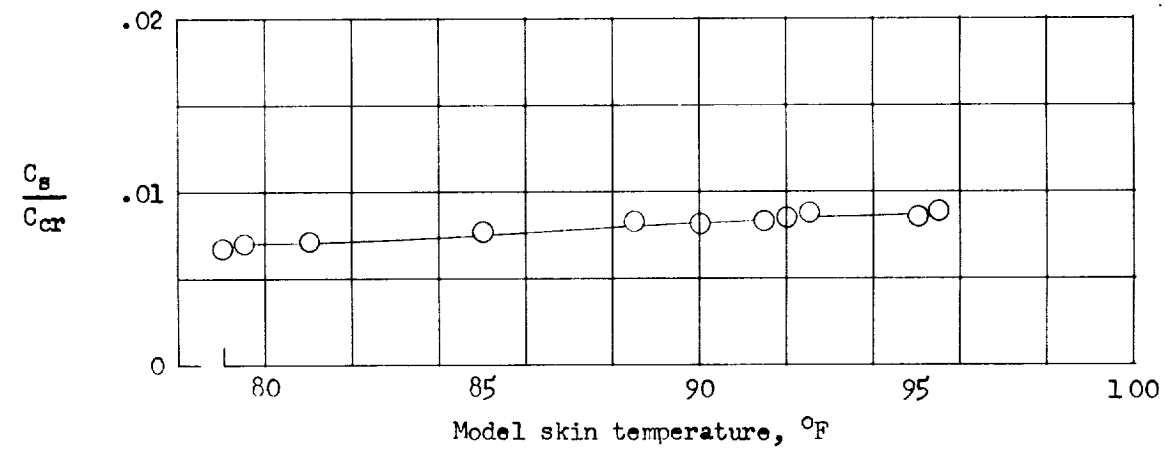

(b) Variation of structural damping coefficient with model skin temperature for constant model amplitude.

Figure 7.- Representative structural damping calibration curves.

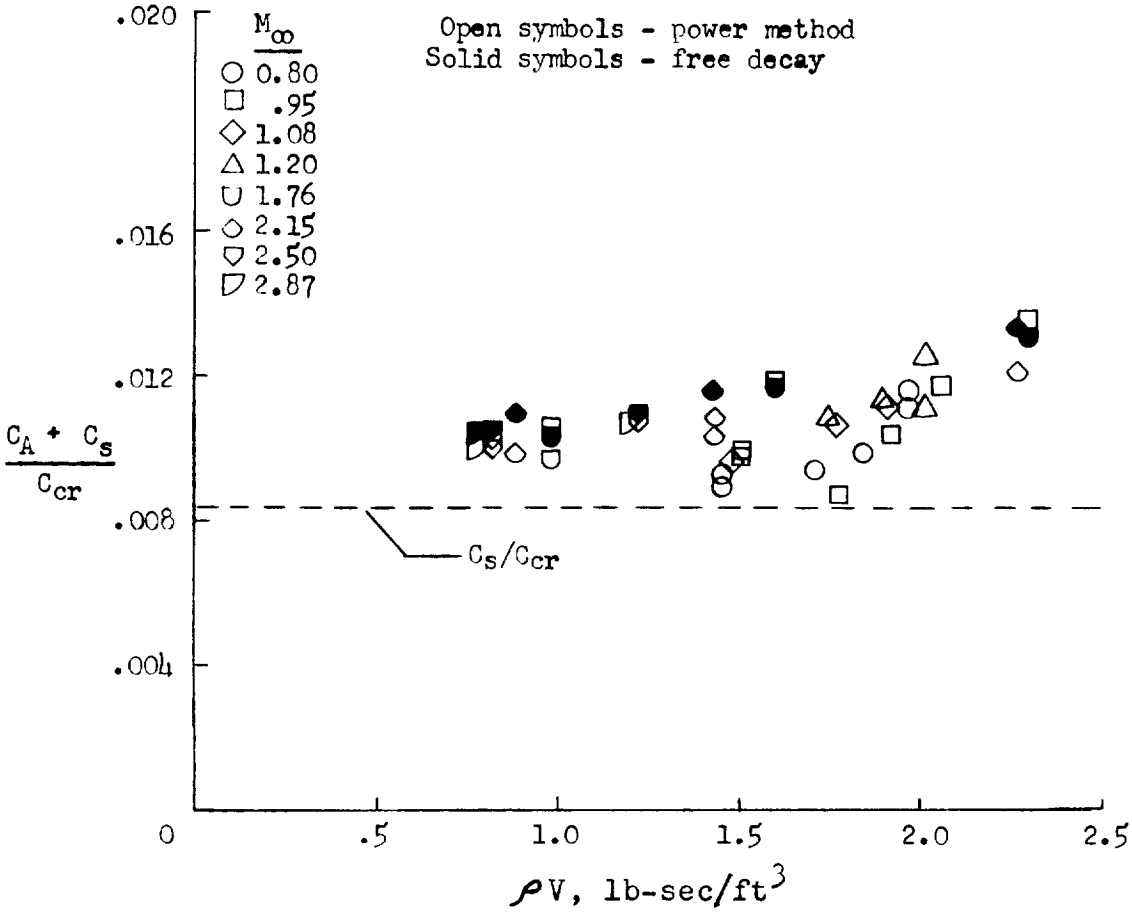

(a) Variation of total damping ratio with flow parameter.

Figure 8.- Damping measurements on model configuration 1 vibrating in the first free-free mode.

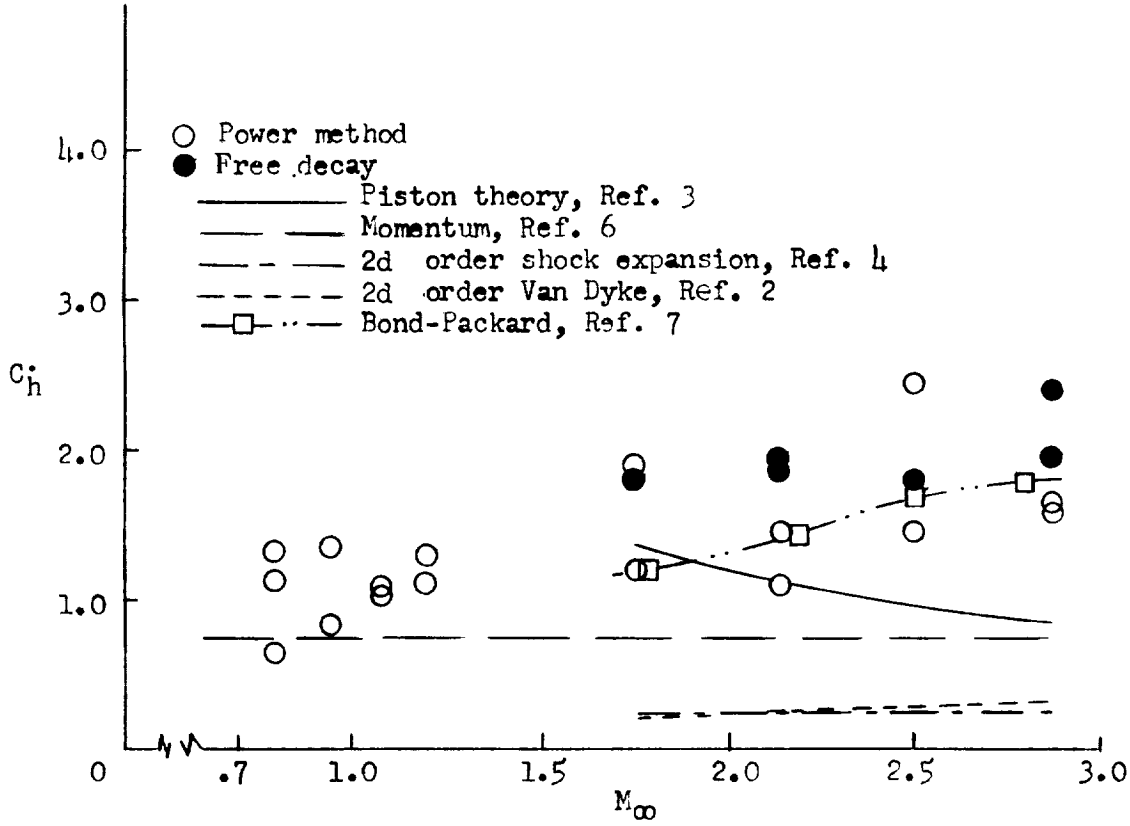

(b) Variation of aerodynamic damping derivative with Mach number.

$$\frac{C_A}{C_{cr}} = C_h^{\cdot} \frac{1}{2\mu k}.$$

Figure 8.- Concluded.

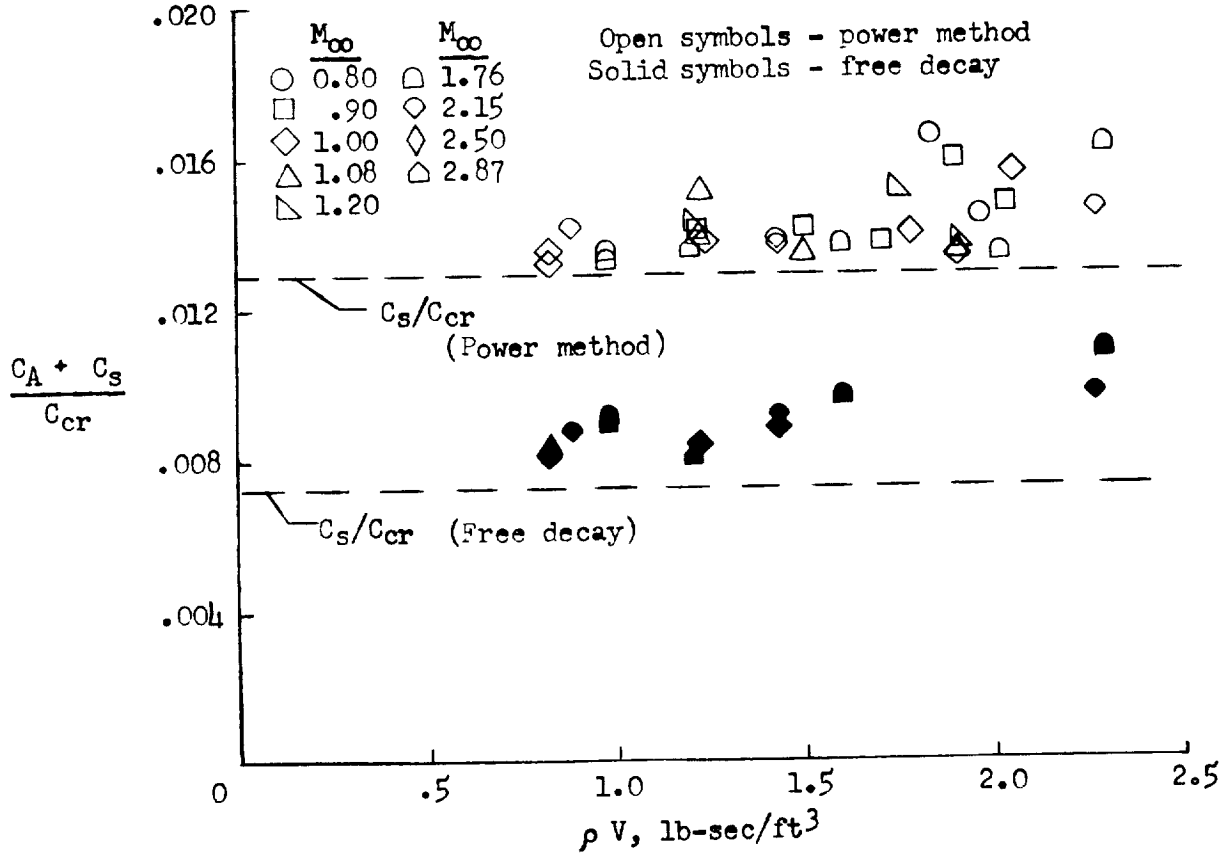

(a) Variation of total damping ratio with flow parameter.

Figure 9.- Damping measurements on model configuration 1 vibrating in the second free-free mode.

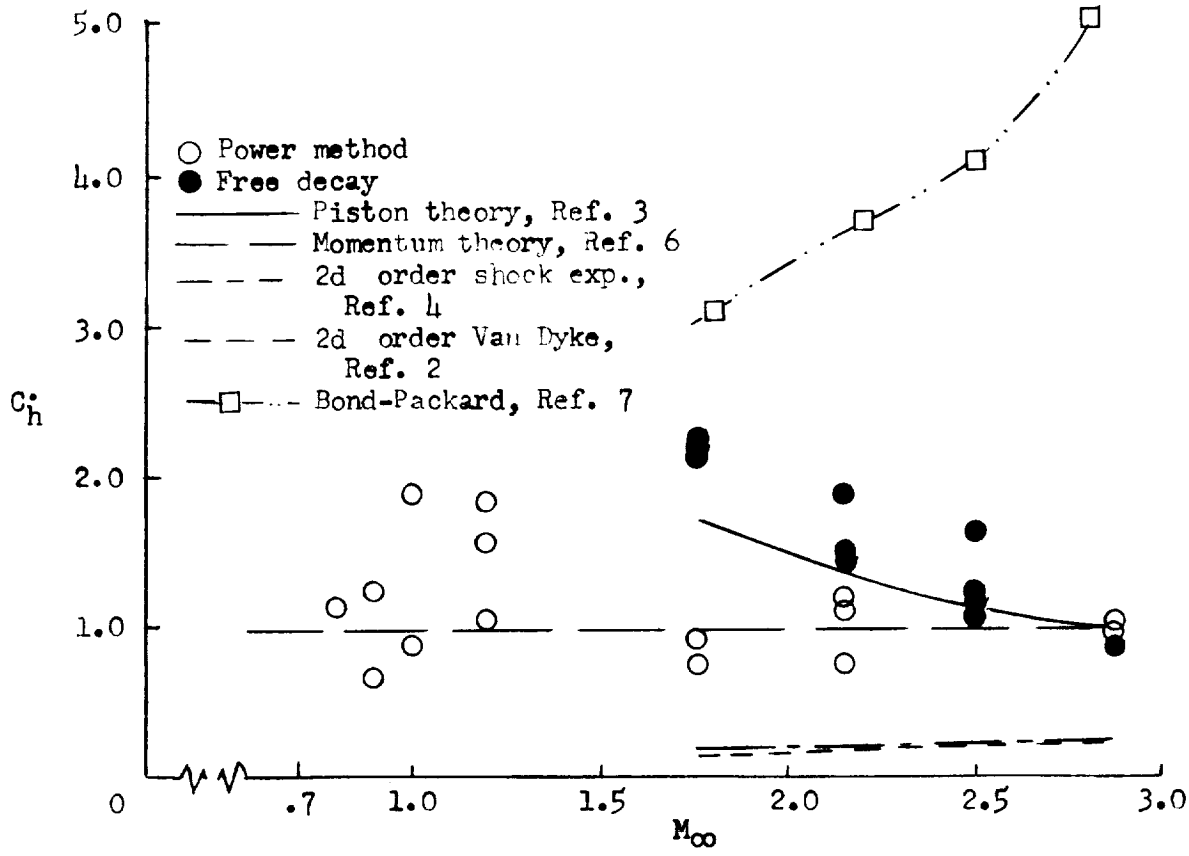

(b) Variation of aerodynamic damping derivative with Mach number.

$$\frac{C_A}{C_{cr}} = C_h^{\cdot} \frac{1}{2\mu k}$$

Figure 9.- Concluded.

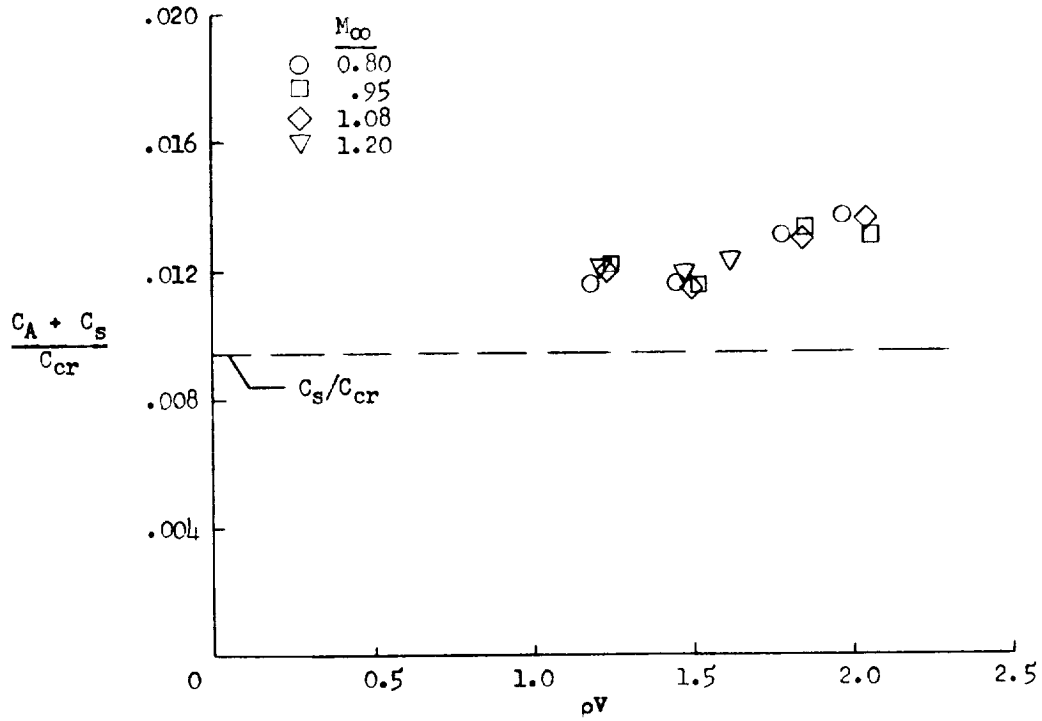

(a) Variation of total damping with flow parameter. Power method.

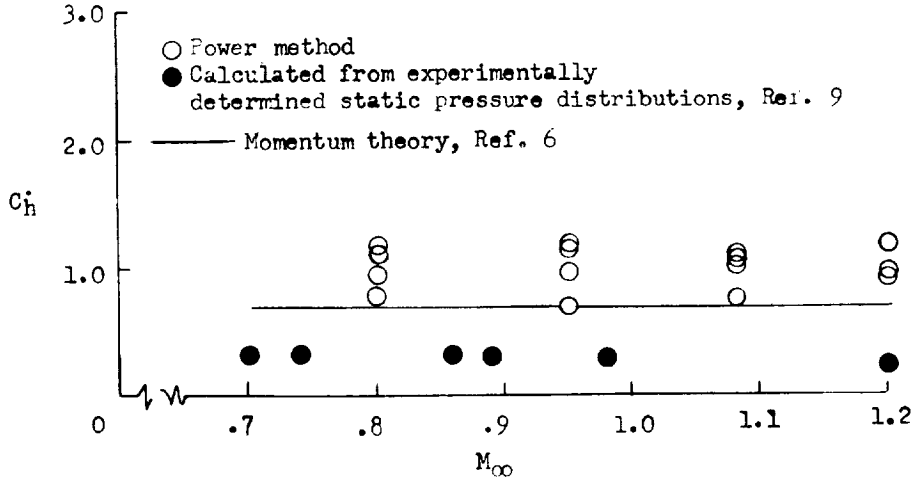

(b) Variation of aerodynamic damping derivative with Mach number.

Figure 10.- Results of damping measurements on model configuration 2 vibrating in the first free-free mode.

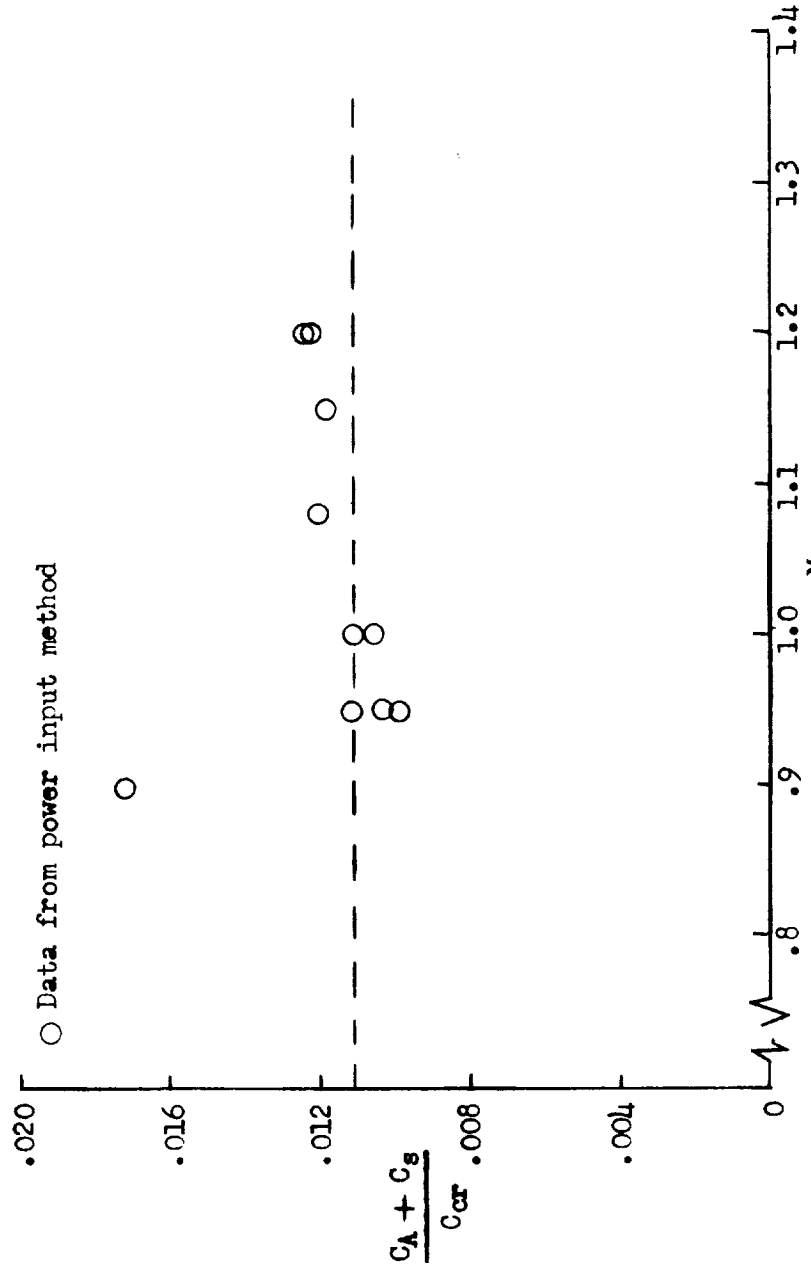

Figure 11.- Variation of total damping with Mach number for model configuration 3 vibrating in first free-free mode.